J. Fluid Mech. (2012), *vol.* 696, *pp.* 374–401.
doi:10.1017/jfm.2012.55

Stability characteristics of a counter-rotating unequal-strength Batchelor vortex pair

Kris Ryan†, Christopher J. Butler and Gregory J. Sheard

Fluids Laboratory for Aeronautical and Industrial Research (FLAIR), Department of Mechanical and Aerospace Engineering, Monash University, VIC 3800, Australia

(Received 13 April 2011; revised 6 November 2011; accepted 23 January 2012; first published online 6 March 2012)

A Batchelor vortex represents the asymptotic solution of a trailing vortex in an aircraft wake. In this study, an unequal-strength, counter-rotating Batchelor vortex pair is employed as a model of the wake emanating from one side of an aircraft wing; this model is a direct extension of several prior investigations that have considered unequal-strength Lamb–Oseen vortices as representations of the aircraft wake problem. Both solution of the linearized Navier–Stokes equations and direct numerical simulations are employed to study the linear and nonlinear development of a vortex pair with a circulation ratio of $\Lambda = -0.5$. In contrast to prior investigations considering a Lamb–Oseen vortex pair, we note strong growth of the Kelvin mode $[-2, 0]$ coupled with an almost equal growth rate of the Crow instability. Three stages of nonlinear instability development are defined. In the initial stage, the Kelvin mode amplitude becomes sufficiently large that oscillations within the core of the weaker vortex are easily observable and significantly affect the profile of the weaker vortex. In the secondary stage, filaments of secondary vorticity emanate from the weaker vortex and are convected around the stronger vortex. In the tertiary stage, a transition in the dominant instability wavelength is observed from the short-wavelength Kelvin mode to the longer-wavelength Crow instability. Much of the instability growth is observed on the weaker vortex of the pair, although small perturbations in the stronger vortex are observed in the tertiary nonlinear growth phase.

Key words: vortex dynamics, vortex instability, vortex interaction

1. Introduction

The production of coherent vortices is an inescapable feature of nearly all practical fluid flows. Understanding the mechanisms governing the development and dissipation of vortex cores has application at nearly all scales of flow, from the development of micro-scale turbulence to the dissipation of synoptic-scale flow structures. Given the wide breadth of application, it is no surprise that this field has generated significant interest for many years – see e.g. the review by Kerswell (2002).

A stable vortex is made susceptible to the growth of both elliptic (Kelvin mode) instabilities and sinuous (Crow) instabilities through the addition of an external strain field. The presence of a neighbouring vortex, parallel to the vortex of interest, induces such a strain field, allowing for the growth of cooperative instabilities to develop on each vortex core. In the absence of an external strain field, perturbations rotate around

† Email address for correspondence: kris.ryan@eng.monash.edu.au

the base vortex, with no growth or decay in amplitude (Kelvin 1880). The external strain field can act to halt the rotation of the perturbation field, while simultaneously amplifying the perturbation.

The Crow instability manifests as a sinuous instability whose axial wavelength is typically far larger than the initial separation distance of the vortex cores. It was first analytically described for a counter-rotating vortex pair of equal circulation magnitude by Crow (1970). Crow demonstrated, using a vortex filament model, that the linear growth of the mode manifested as a symmetric oscillation that grows on each vortex at a 45° inclination to an imaginary line drawn between each unperturbed vortex. Crow's (1970) analysis was subsequently extended by Widnall, Bliss & Tsai (1974), who corrected an asymptotic simplification in Crow's study, allowing the model to be extended to correctly predict instabilities at higher wavenumbers. The vortex filament model has been extended to consider a co-rotating vortex pair by Jimenez (1975) and Bristol *et al.* (2004), who independently demonstrated that the instability could not develop for such a case. Crouch (1997) and Fabre, Jacquin & Loof (2002) have further extended the model to consider the effect of multiple vortex filaments, reminiscent of the wake of an aircraft.

For a counter-rotating vortex pair of equal circulation magnitude, the late-stage development of the Crow instability leads to the initially parallel vortex cores connecting periodically along their axis, and the system transforms into a series of vortex rings – see e.g. Scorer & Davenport (1970) and Garten *et al.* (2001). The processes underpinning the late-stage development have only recently been quantified by Leweke & Williamson (2011). By contrast, for counter-rotating vortex pairs of unequal circulation magnitude, large-wavelength Crow perturbations emanating from the weaker vortex wrap around the stronger vortex during nonlinear development (see Marshall, Brancher & Giovannini 2001; Ortega, Bristol & Savaş 2003; Bristol *et al.* 2004).

By contrast to the Crow instability, an elliptic instability can exhibit a positive growth for both co- and counter-rotating vortex pairs – see e.g. the experimental findings of Leweke & Williamson (1998) and Meunier & Leweke (2005). The axial wavelength of an elliptic instability is typically of the same order as the vortex core radius. Given this scaling, the instability is dependent on the local features of the unperturbed vortex profile, and hence a filament analysis similar to that proposed by Crow (1970) is insufficient for the description of the mode. Tsai & Widnall (1976) conducted a first-order analysis for a Rankine vortex immersed within an infinitesimal strain field; independently, Moore & Saffman (1975) provided an analytical framework for a generic vortex profile. Subsequent investigations have considered the growth of elliptic instabilities for a variety of vortex profiles, including the Burgers and Lamb–Oseen profiles (Eloy & Le Dizès 1999), the addition of an axial velocity to the Rankine vortex profile (Lacaze, Birbaud & Le Dizès 2005) and a Batchelor vortex (Lacaze, Ryan & Le Dizès 2007). The analytical framework describing the development of short-wave, elliptic instabilities has been summarized by Kerswell (2002).

These investigations have shown that the elliptic instability is amplified due to the coupling of a pair of Kelvin modes, which, while neutrally stable for an isolated vortex, resonate with an externally imposed strain field. The Kelvin mode pair are restricted to having the same axial wavenumber in addition to their azimuthal wavenumbers being restricted, such that, if one Kelvin mode has azimuthal wavenumber m_i, the second Kelvin mode must have an azimuthal wavenumber $m_{ii} = m_i \pm 2$. (We refer to mode couplings in the generic form $[m_i, m_{ii}, n]$ throughout.

Note that n refers to the branch number of the mode coupling – see e.g. Saffman (1992) for further details.) The elliptic instability process is tuned to a select normalized axial wavenumber $\kappa = ka$ (where k is the axial wavenumber and a describes the vortex core radius). Away from this axial wavenumber, the process is detuned, leading to a reduction in the growth rate. Eloy & Le Dizès (1999) provided an analytical framework to describe this detuning process.

Eloy & Le Dizès (1999) point out that the detuning process has important implications for the nonlinear development of elliptic instabilities. Coupled with the viscous diffusion, which increases the vortex radius as a function of time, the critical normalized axial wavenumber changes as a function of time. Over time, the growth rate will reduce at a given wavenumber, reducing the growth rate as the instability alters the structure of the base vortex pair.

Numerous studies have investigated the stability of vortex pairs to the combined effects of both Crow and elliptic mode perturbations. Leweke & Williamson (1998), in their investigation of an equal-strength counter-rotating Lamb–Oseen vortex pair, identified the development of both an elliptic mode (consisting of a coupling of Kelvin modes with azimuthal wavenumber $[-1, 1]$) and the large-wavelength Crow instability. They noted that the presence of both modes significantly enhanced the dissipative effect that may be provided by either mode in isolation. Importantly, they observed the development of a series of transverse, counter-rotating 'secondary vortex' pairs during the nonlinear growth phase of the instability. These secondary vortices transfer energy from one vortex to its neighbour, enhancing mixing and promoting dissipation of both vortices. Through dye visualizations, Leweke & Williamson (1998) observed two secondary vortex tubes originating per Kelvin mode $[-1, 1]$ wavelength. Direct numerical simulation (DNS) conducted by Laporte & Corjon (2000) verified these findings. Recently, Schaeffer & Le Dizès (2010) detailed the nonlinear dynamics for a mode $[-1, 1]$ for a Lamb–Oseen vortex.

A counter-rotating vortex pair of equal circulation magnitude represents a unique situation, where both vortices travel with a constant velocity perpendicular to an imaginary line drawn between the two vortices. As is well understood (see e.g. Le Dizès & Laporte 2002), in general, a vortex pair will rotate about a fixed point. In this situation, both vortices will observe a rotating strain field. For both Crow and Kelvin modes, this global rotation rate alters the κ for optimal tuned growth, the mode shape and the growth rate of the perturbation. This effect was investigated by Le Dizès & Laporte (2002) and So, Ryan & Sheard (2011) for a Lamb–Oseen vortex pair for the case of elliptic instabilities and by Bristol *et al.* (2004) for Crow instabilities.

More recent investigations have considered a Batchelor vortex in an externally induced strain field. The Batchelor vortex is the asymptotic solution to the linearized Navier–Stokes equation for a trailing line vortex profile far downstream of an aircraft (Batchelor 1964), and is therefore a closer approximation to an experimental aircraft wake than the Lamb–Oseen vortex profile. In particular, the Batchelor vortex incorporates an axial velocity component, which has the potential to lead to instability growth on an isolated vortex, without the need for an externally imposed strain field. Both inviscid modes and viscous modes (whose growth rate diminishes as $Re \to \infty$) have been shown to occur. Several authors have shown that it is the relative strength of the axial velocity to azimuthal velocity that determines the stability of an isolated Batchelor vortex (see e.g. Ash & Khorrami 1995). An isolated Batchelor vortex with low axial velocity magnitude has been shown to be stable in the inviscid framework. A recent study by Heaton (2007) has shown that instabilities develop even for small

axial velocities, but their growth rate is considerably smaller than that found for the elliptical modes under investigation.

Lacaze *et al.* (2007) have shown that a counter-rotating, equal-strength Batchelor vortex pair (with small axial velocity) leads to the growth of more complex short-wave mode shapes in preference to the Kelvin mode $[-1, 1]$. These modes may also be described in terms of alternative Kelvin mode couplings. In particular, mode $[-2, 0]$ and mode $[-3, -1]$ have been shown to grow in the presence of an axial velocity, the preferred instability mode being dependent on the ratio of axial velocity to the swirl velocity. DNS conducted by Ryan & Sheard (2007) considered the development of the $[-2, 0]$ mode on a Batchelor vortex pair of equal circulation strength. For a sufficiently high axial velocity component, this mode has approximately the same linear growth rate as the $[-1, 1]$ mode for a Lamb–Oseen vortex pair (Lacaze *et al.* 2007; Roy *et al.* 2008). By contrast to prior findings for a Lamb–Oseen vortex pair, the nonlinear dissipation of the Batchelor vortex pair was muted, with negligible improvements in dissipation rates beyond two-dimensional dissipation. The investigation failed to identify the formation of secondary vortices during the nonlinear phase of growth; Ryan & Sheard (2007) suggested that the perturbation mode shape was not conducive to the formation of secondary vortices. Recent work by Roy *et al.* (2011) compared the growth of short-wave instabilities on co- and counter-rotating vortex pairs of equal circulation strength. They demonstrated, through dye visualization, the growth of both mode $[-2, 0, 1]$ and (for the counter-rotating vortex pair) the Crow instability. Their experiment confirmed prior analytical and simulated results for Batchelor vortex pairs.

Given the significant differences noted for an equal-strength Batchelor vortex pair (when compared with a Lamb–Oseen vortex pair), it is highly improbable that prior studies on the evolution of unequal-strength Lamb–Oseen vortex pairs would have findings directly comparable to an unequal-circulation-strength Batchelor vortex pair. This study extends previous investigations by considering a Batchelor vortex pair with low axial velocity and circulation strength ratio $\Lambda = -0.5$; it is reasoned that the fundamental physics describing the evolution of this vortex pair is representative of a wide range of unequal-strength circulation ratios.

This paper is organized as follows. Section 2 provides details of the model being considered. The numerical techniques employed are defined in § 4, while a description of the numerical domain under consideration is described in § 5. The two-dimensional relaxation of the vortex pair is described in § 6.1, before linear stability analysis findings (§ 6.2) and DNS findings (§§ 6.3–6.6) are described.

2. Objective

This study considers a relatively simple system comprising two Batchelor vortices of unequal circulation strength. The vortices are separated by a distance b and have a characteristic radius a. In general, a Batchelor vortex is defined completely as

$$\omega_{xy} = \frac{\Gamma}{\pi a^2} \mathrm{e}^{-(r/a)^2}, \tag{2.1}$$

$$W = \frac{W^* a_0 \, |\Gamma|}{2\pi a^2} \mathrm{e}^{-(r/a)^2}, \tag{2.2}$$

where ω_{xy} is the axial vorticity field, W the axial velocity field, Γ the circulation, r the radial distance away from the vortex core, and W^* the axial velocity coefficient. Note that a_0 represents the initial characteristic core radius; as the vortex evolves, the

characteristic radius increases due to diffusion, and (to first approximation) may be determined at any time t from

$$a = \sqrt{a_0^2 + 4\nu t}, \tag{2.3}$$

where ν is the fluid kinematic viscosity.

Three key parameters have previously been shown to control the growth rate in an equal-strength Batchelor vortex pair (Lacaze *et al.* 2007), namely the Reynolds number, defined as $Re = \Gamma/\nu$, the external strain rate, ε_{ext}, and the axial velocity coefficient, W^*. The external strain rate describes the strain acting on a vortex purely by the presence of its neighbour. It is proportional to both the separation distance of the vortices and the circulation of the adjacent vortex, and may be written in non-dimensional form (see e.g. Lacaze *et al.* 2007) as

$$\varepsilon_{ext} = \frac{S_{ext}}{\Omega_0} = \left(\frac{a}{b}\right)^2 \frac{\Gamma_{adj}}{\Gamma_i}, \tag{2.4}$$

$$S_{ext} = \frac{\Gamma_{adj}}{2\pi b^2}, \tag{2.5}$$

$$\Omega_0 = \frac{\Gamma_i}{2\pi a^2}, \tag{2.6}$$

where S_{ext} is the dimensional form of the external strain rate, Ω_0 is the rotation induced by the vortex at its centre, Γ_{adj} is the circulation of the adjacent vortex, and Γ_i is the circulation of the vortex of interest. As described by Le Dizès & Laporte (2002), the strain rate actually measured at the vortex core is dependent on both ε_{ext} and the profile of the vortex core in question. The growth rate of the elliptic instability may be shown to be proportional to this internal strain rate, ε_{int}. For vortices of Gaussian profile, Le Dizès & Laporte (2002) have shown that ε_{int} may be related to ε_{ext} as

$$\varepsilon_{int} = \left[1.5 + 0.038\left(0.16 - \frac{\Gamma_i + \Gamma_{adj}}{2\Gamma_{adj}}\left(\frac{a}{b}\right)^2\right)^{-9/5}\right]\varepsilon_{ext}. \tag{2.7}$$

An additional controlling parameter considered in this study is the circulation ratio, $\Lambda = \Gamma_1/\Gamma_2$ (note that, for any given variable ϕ, ϕ_1 refers to the weaker vortex and ϕ_2 to the stronger vortex throughout). As discussed in § 1, a value of Λ away from $\Lambda = -1$ will induce a global rotation of the vortex pair, which will alter the growth of the instability modes away from that predicted for $\Lambda = -1$. In addition, we have assumed that the peak axial velocity passing through the two vortices is equal. Given that both vortices have the same maximum axial velocity, an unequal circulation ratio implies an unequal axial velocity coefficient through the definition

$$\frac{W_2^*}{W_1^*} = |\Lambda|. \tag{2.8}$$

From consideration of figure 9 in Lacaze *et al.* (2007), we anticipate that it is possible, if not likely, that an unequal-strength Batchelor vortex pair will exhibit different modes of instability growth on each vortex core across a wide range of Λ values for moderate axial velocity magnitudes. That is, the Kelvin mode coupling, which is most unstable on one vortex, will differ from that on the neighbouring vortex, simply due to the variation in axial velocity coefficient.

For this study $Re = 2800$ and a separation distance $a_0/b = 0.25$ was chosen (note that this implies that both vortices initially have the same characteristic radius a_0). We

consider a value of $\Lambda = -0.5$ and a maximum axial velocity coefficient of $W_1^* = 0.3$ (as such, $W_2^* = 0.15$). These values have been chosen because, when considering the analytical work described in Lacaze *et al.* (2007), they provide the best opportunity to observe significant perturbation growth across both vortices. In addition, we note that an isolated Batchelor vortex with these values of W^* would be stable to three-dimensional perturbations (see Lacaze *et al.* 2007, and references therein).

Considering the work of Lacaze *et al.* (2007) we predict *a priori* that a Kelvin mode $[-2, 0, 1]$ will dominate the weaker vortex, while a Kelvin mode $[-1, 1, 1]$ will be observed on the stronger vortex. A Crow instability should develop on both vortices. Given the substantially lower value of ε_i anticipated in the stronger vortex, much of the perturbation growth is anticipated on the weaker vortex.

3. Approach

Two methods were employed to simulate the vortex system. The first technique predicts which linear modes will become most unstable through solution of the linearized Navier–Stokes equations. Using this technique, numerical modelling is performed in two stages. Initially, the time-dependent two-dimensional flow field is predicted through the solution of the two-dimensional Navier–Stokes equations. This allows the vortex system to 'relax' to a solution of the Navier–Stokes equations. The system is then frozen, and the linearized Navier–Stokes equations are then solved in a rotating reference frame to determine the stability of the two-dimensional system to three-dimensional disturbances. This technique is identical to that previously used by So *et al.* (2011) to consider the growth of instabilities of an unequal-strength Lamb–Oseen vortex pair.

The second technique employed DNS to validate the stability analysis findings, and to investigate the nonlinear growth of the instabilities. The DNS investigation was initialized by superimposing two Batchelor vortices separated by a distance b. The relaxation of the vortex pair was simulated in three-dimensional space. As has been shown by both Sipp, Jacquin & Cossu (2000) and Le Dizès & Verga (2002) (and verified in both §§ 6.1 and 6.3.1), relaxation of the vortex pair occurs over a very short period of time, which is significantly less than the time scale over which linear perturbations grow.

4. Numerical techniques employed

Our simulations solve the three-dimensional incompressible Navier–Stokes equations in primitive variable form:

$$\frac{\partial \boldsymbol{u}}{\partial t} + (\boldsymbol{u} \cdot \nabla)\,\boldsymbol{u} = -\nabla P + \nu \nabla^2 \boldsymbol{u}, \tag{4.1}$$

$$\nabla \cdot \boldsymbol{u} = 0, \tag{4.2}$$

where $\boldsymbol{u}$ is the velocity vector and P is the kinematic pressure. The linear stability analysis technique solves the linearized form of (4.1) and (4.2) (as described by Sheard, Fitzgerald & Ryan 2009), whereas the DNS technique solves (4.1) and (4.2) directly.

For both the DNS and linear stability analysis investigations, a spectral-element method was employed to spatially discretize the relevant form of (4.1) and (4.2) in the plane normal to the axes of the vortex pair. High-order Gauss–Legendre–Lobatto polynomials were used as interpolants within each macro-element, and spatial accuracy was determined by choosing the order of the tensor product of these polynomials. This

technique, described in detail by Karniadakis & Sherwin (2005), has the significant advantage of near spectral convergence, while allowing controllable mesh density as per finite element methods.

Time integration was performed using a third-order accurate operator splitting scheme based on backwards differencing (Karniadakis, Israeli & Orszag 1991). The algorithm has been described in a number of previous investigations, notably Sheard *et al.* (2009) for DNS simulations and So *et al.* (2011) for linear stability analysis.

4.1. *The direct numerical simulation technique*

The DNS technique employs a Fourier/spectral-element method to spatially resolve the domain in the third dimension. Here, the flow field at each point on the two-dimensional grid is described by a Fourier expansion in the axial direction. In the formulation employed, the Fourier modes are only coupled during the advection sub-step; the pressure and diffusion sub-steps are computed in a decoupled fashion. This leads to a significant advantage for parallel simulations over fully three-dimensional spectral-element simulations. This approach has been employed previously for a wide variety of simulations – see e.g. Karniadakis & Triantafyllou (1992), Thompson, Hourigan & Sheridan (1996) and Blackburn & Sherwin (2004) among many others. The global spectral approach has the advantage of pseudo-spectral convergence, but the boundary conditions in the axial direction are restricted to be periodic.

4.2. *The linear stability analysis technique*

Linear stability analysis determines the stability of a two-dimensional base flow field to perturbations of a predetermined axial wavenumber. The linear stability analysis technique solves the linearized form of (4.1) and (4.2); this linearized form differs from the full three-dimensional Navier–Stokes equations only in the advection term, and thus an almost identical algorithm can be employed as described for the DNS technique. Importantly, the technique assumes a time-independent base flow field. However, for a finite Reynolds number, an unequal-strength vortex pair will evolve due to dissipative effects. To overcome this problem, the base flow field is frozen at the conclusion of the relaxation period (see § 6.1). Owing to the rotation of the vortex pair, freezing the base flow field requires the perturbation field to be evolved within a rotating reference frame that matches the base flow field. This rotation of the perturbation field ensures that the Coriolis forces induced by the rotation of the base vortex pair are accounted for. Thus, in the rotating reference frame, the base flow field is modelled as steady-state after the conclusion of the relaxation phase.

For T-periodic base flow fields (of which a steady-state base flow field is a special example), the perturbation field evolves over one period subject to an operator $\boldsymbol{A}$ as

$$\boldsymbol{u}'_{t+T} = \boldsymbol{A}(\boldsymbol{u}'_t), \tag{4.3}$$

where $\boldsymbol{u}'_t$ represents any one of the perturbation velocity components or perturbation pressure field calculated at time t. The eigenvalues to this problem may be written as

$$\mu = \exp(\sigma T), \tag{4.4}$$

where σ corresponds to the growth rate of the instability.

Owing to the size of the systems under investigation, $\boldsymbol{A}$ is not constructed explicitly. Instead, the base flow and perturbation field are integrated in time and leading eigenvalues are determined using an implicitly restarted Arnoldi method. This scheme has been validated against an independent implementation by Blackburn & Sheard

(2010), while the work of Sheard *et al.* (2009) validated the scheme against DNS results and experimental findings.

4.3. *Potential limitations of the direct numerical simulation technique*

The Fourier decomposition of the Navier–Stokes equations in the axial direction restricts the model to only consider periodic boundary conditions in the axial extent; this may lead to results that differ from those observed experimentally. Previous investigations have shown that the critical wavelength of Crow instabilities scales with the separation distance of the two vortices $\kappa_{Crow} = kb$, while the shorter-wavelength Kelvin modes scale with the vortex core radii $\kappa_{Kelvin} = ka$.

The increase in the vortex core radius over time, equation (2.3), will increase κ_{Kelvin}, leading in a decrease in the growth rate predicted from the DNS simulation away from that predicted from linear investigations (Eloy & Le Dizès 1999). This effect may be minimized by increasing the Reynolds number of the simulation (hence decreasing the viscous growth of the vortex radii) and increasing the number of Kelvin mode instability wavelengths contained within the axial extent of the domain. In the present study, eight Kelvin mode instability wavelengths and three Crow instability wavelengths were contained within the domain.

5. Computational details

A circular domain of radial extent $100a_0$ was employed in the x–y plane for all simulations described herein. The vortex pair was modelled in the centre of the domain within a highly resolved portion of the mesh. The highly resolved region had an extent $23a_0 \times 23a_0$, and comprised square macro-elements. The extent of the highly resolved region was determined through several trial simulations. Reducing the size of the highly resolved region led to advection of vortex filaments outside of this region during late stages of nonlinear growth in DNS simulations.

The number of macro-elements required for the simulation was determined through an h-type resolution study, whereby the effect of macro-element size was considered. In the refined region, macro-elements of width $\Delta x = 0.5a_0$ through to $\Delta x = 1.2a_0$ were considered. For each mesh, the Lagrangian polynomial interpolant order chosen was $p = 9$. The internal strain rate, ε_{int}, and the peak vorticity measured at the core of each vortex were calculated at the conclusion of the relaxation phase for each mesh. Variations of less than 1 % were observed between $\Delta x = 0.5$ and $\Delta x = 0.8$ for all variables considered. Subsequently, the central refined region consisted of square elements each of width $\Delta x = 0.8a_0$. Away from the resolved region, the mesh density decreased with increasing radius. The domain extent chosen was found to be sufficient, such that the non-slip wall boundary conditions imposed at the perimeter of the domain did not influence the development of the vortex pair. Overall, the mesh was composed of 589 quadrilateral conforming elements.

In addition to the h-type resolution, mesh independence was established by performing a p-type resolution study whereby the order of the Lagrangian polynomial interpolants within each element was successively increased until the solution was mesh-independent. Both the development of the two-dimensional base field and the perturbation growth rate of the two leading modes (investigated at $ka = 2.5$) were modelled as a function of p. The perturbation growth rate was compared, as the perturbation field typically yields spatially smaller-scale structures than the base flow field – and thus gives a more accurate indication of the mesh resolution required. As with the h-type resolution study, the internal strain rate, ε_{int}, and the peak vorticity

measured at the core of each vortex were calculated at the conclusion of the relaxation phase. Variations of less than 1 % were observed between $p = 12$ and $p = 15$ for all variables considered. An eleventh-order ($p = 12$) Lagrangian polynomial interpolant was used for the tensor-product expansion basis for all subsequent calculations.

The DNS investigations considered an axial extent of $27.25 \times a_0$. This allowed for three wavelengths of the large-wavelength Crow instability and eight wavelengths of the Kelvin mode to be captured within the domain. Section 6.2 details the critical wavelengths of both these modes as predicted from the linear stability analysis, which directed the axial domain extent of the DNS investigation.

In all, 80 Fourier modes were calculated in the axial direction, allowing for eight Fourier modes to resolve each Kelvin mode and 27 Fourier modes to describe each Crow mode. During the DNS investigation, the highest Fourier mode was monitored to ensure that any aliasing was limited. At the transition to nonlinear growth (where any effect of aliasing was noted to be highest), the kinetic energy within the highest Fourier mode was measured at $\simeq 4 \times 10^{-6}$. This was $O(10^{-6})$ times the energy measured for the Kelvin mode, $O(10^{-7})$ times the energy measured for the Crow mode, and $O(10^{-9})$ times the energy of the fundamental $m = 0$ mode.

6. Results

6.1. *Two-dimensional relaxation of the base flow field*

The two-dimensional base flow is initialized simply by superimposing two Batchelor profile vortices a distance b apart. As is well documented, two superimposed Batchelor profile vortices are not a solution to the Euler equations and as a result undergo a rapid adaptation period. The adaptation phase was shown to be dominated by inviscid forces by Le Dizès & Verga (2002) for co-rotating vortices and by Sipp *et al.* (2000) for counter-rotating vortices, and involves each vortex in the vortex pair evolving from a circular profile to an elliptical one. The evolution involves the oscillation in the profile of each vortex and may be monitored by considering ε_{int} measured within each vortex core. As the vortex pair adapt to the Euler solution, oscillations in ε_{int} decay. The critical time after which the base field is said to have adapted is determined through monitoring the oscillations of ε_{int} as a function of time. Both Sipp *et al.* (2000) and Le Dizès & Verga (2002) found that the time scale for adaptation was directly dependent on the circulation of the vortex. As they only considered equal-strength vortices, only one time scale was appropriate. However, in our case, two time scales may be defined, as each vortex has a different circulation.

Figure 1 shows ε_{int} measured within each vortex core as a function of normalized time. Following Le Dizès & Verga (2002), time has been normalized using the definition

$$t^*_{nv} = \frac{t|\Gamma_i|}{2\pi a_0^2}, \tag{6.1}$$

where the subscript nv indicates that this is a non-viscous normalization in time and Γ_i is the circulation of the vortex in question. The negative, weaker vortex is seen to exhibit significantly higher-amplitude oscillations when compared to the stronger, positive vortex. This is expected owing to the significantly higher local strain experienced by the weaker vortex. Both vortices appear to conclude the adaptation process by $t^*_{nv} \simeq 30$. When considering (6.1), this is seen to imply that it takes significantly longer for the weaker vortex to adapt. Given the significantly higher strain to which the weaker vortex must adapt, this is not surprising.

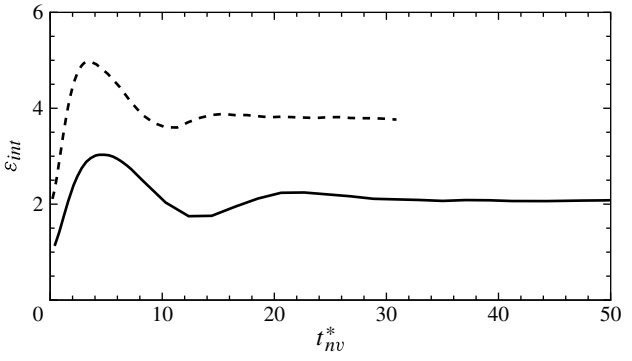

FIGURE 1. Internal strain-rate magnitude (ε_{int}) as a function of normalized time t^*_{nv}, measured at the core of each vortex; —, stronger vortex; – –, weaker vortex.

	Γ	Re	ε_{int}	ε_{ext}	W^*	a
Γ_1	−46.03	1282.0	−0.539	−0.273	0.311	1.09
Γ_2	96.32	2682.7	0.136	0.062	0.154	1.09

TABLE 1. Parameter values at the conclusion of the relaxation period ($t^*_{nv} = 30$ based on the weak vortex); Γ_1 refers to the weaker vortex and Γ_2 refers to the stronger vortex.

Viscous diffusion of the vortices results in increasing overlap of the vortices as a function of time. The effect is driven purely by viscous diffusion, and may be modelled to first approximation by superimposing two circular vortices a distance b apart and allowing for viscous diffusion in the absence of relaxation. Over long periods of time, the Reynolds number, based on the circulation of the vortex in question, was found to reduce exponentially. However, over the short time periods investigated in this study (including the entirety of the DNS results discussed later), the variation in Reynolds number is well approximated as a linear reduction with time. Table 1 details Re, ε_{int}, ε_{ext} and W^* for each vortex at the conclusion of the relaxation process ($t^*_{nv} = 30$ based on the weak vortex); in addition, $a/b = 0.361$ at this time. We note that $\varepsilon_{int} \simeq 2\varepsilon_{ext}$, as predicted for this system using (2.7).

The axial vorticity and strain-magnitude fields of the adapted flow field are shown in figure 2, corresponding to $t^*_{nv} = 30$. This is the flow field used as the base flow in the stability analysis study. The strain field is found to be significantly higher within the weaker vortex than the stronger one. This would imply that, for an excited global mode, instability growth should be stronger in the weaker vortex.

6.2. *Linear stability analysis*

Figure 3(*a*) shows the normalized growth rates obtained from the linear stability analysis, as a function of wavenumber. Following the work of Le Dizès & Laporte (2002), the wavenumber is normalized by the vortex core radius (here chosen as the core radius of the strong vortex); and the growth rate has been normalized using the

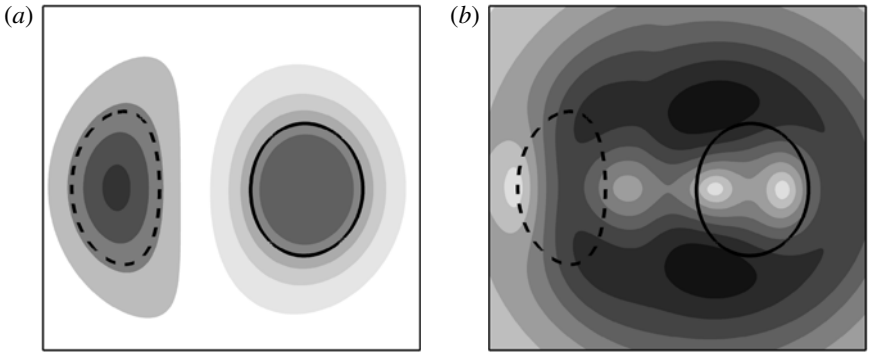

FIGURE 2. (*a*) Vorticity field and (*b*) strain field at the conclusion of the adaptation phase ($t^*_{nv} = 30$). Contour lines show the vortex core radii (*a*) strained from their original radius of a_0; dashed lines indicate negative vorticity. Shaded contours indicate the strength of the field in question; in panel (*a*) darker shading indicates negative vorticity, lighter shading indicates positive vorticity; in panel (*b*) darker shading indicates a stronger magnitude of strain.

global turnover time, where

$$t_G = \frac{4\pi^2 b_0^2}{|\Gamma_1|(1+\Lambda)}, \tag{6.2}$$

is the time taken for the vortex pair to make one revolution about each other. Note that we use the initial separation distance b_0 in (6.2). This leads to two non-dimensional parameters to describe the growth of perturbations,

$$\sigma^* = \sigma \times t_G, \tag{6.3}$$

$$t^* = \frac{t}{t_G}, \tag{6.4}$$

referred to as the normalized growth rate and normalized time, respectively.

Five modes have been identified as growing on the vortex system. Of these, three dominate – having significant growth rates. These are the long-wavelength Crow instability, and the shorter-wavelength Kelvin modes $[-1, 1, 1]$ and $[-2, 0, 1]$. This is in agreement with the predictions of Lacaze *et al.* (2007) and contrasts with the modes that grow on Lamb–Oseen vortex pairs (where only the Crow instability and the Kelvin mode $[-1, 1]$ exhibit positive growth).

The Crow instability has a peak $\sigma^* = 8.67$ at a critical wavenumber of $\kappa_c = ka = 0.75$, in excellent agreement with the analytical predictions of Bristol *et al.* (2004). Using their model, we find a peak $\sigma^* = 8.9$ at a critical wavenumber of $\kappa_c = 0.62$. The mode shape is shown in figure 3(*b*), and is similar in profile to that described previously by many authors – for example, Crow (1970) and Widnall *et al.* (1974) for equal-strength vortices and So *et al.* (2011) for unequal-strength vortices. The perturbation field was found to evolve predominantly in the vicinity of the weaker vortex in preference to the stronger vortex.

Of the short-wavelength (Kelvin) instabilities, mode $[-2, 0, 1]$ is found to dominate over the majority of the wavelengths considered. A peak growth rate of $\sigma^* = 8.5$ at a critical wavenumber of $\kappa_c \simeq 2.4$ was observed. While this peak growth rate is slightly lower than that of the Crow instability, the separation in critical wavenumbers should allow both instabilities to be clearly identifiable experimentally. The mode shape for mode $[-2, 0, 1]$ is shown in figure 3(*c*); a classical mode $[-2, 0, 1]$ shape is observed

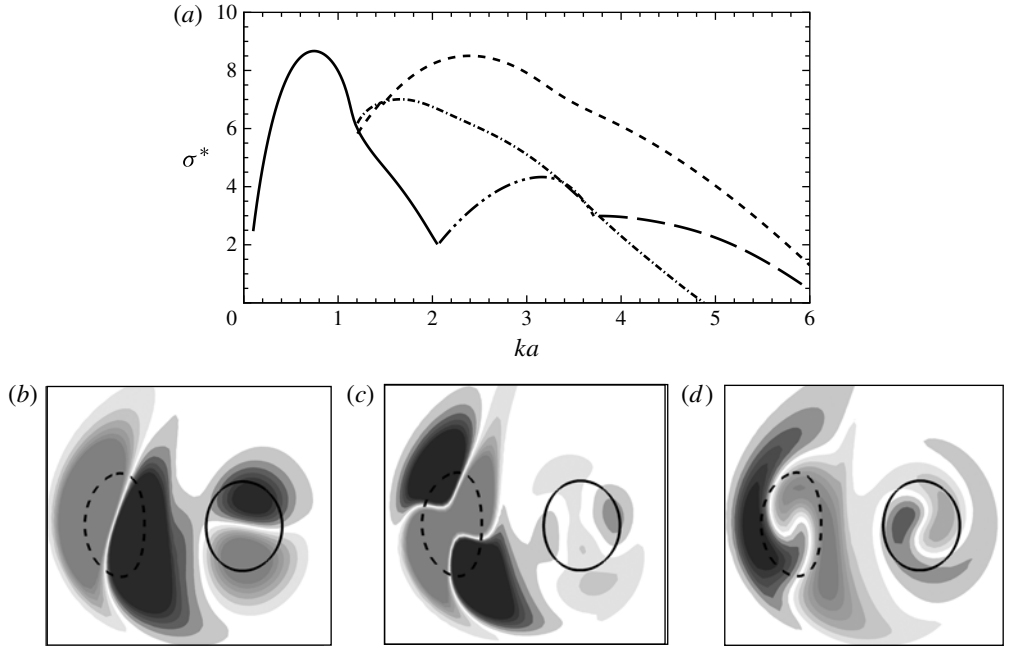

FIGURE 3. (*a*) Growth rate for each of the modes identified in the linear stability analysis, as a function of normalized wavenumber ka. Modes have been identified as: —, large-wavelength Crow instability; – · –, Kelvin mode $[-1, 1, 1]$; - - -, Kelvin mode $[-2, 0, 1]$; – ·· –, Kelvin mode $[-2, 0, 2]$; — — —, Kelvin mode $[-3, -1, 1]$. (*b–d*) Perturbation axial vorticity fields for: (*b*) the Crow instability, (*c*) Kelvin mode $[-2, 0, 1]$, and (*d*) Kelvin mode $[-1, 1, 1]$. In each case, shaded contours are of the perturbation field; lightly shaded regions indicate a positive perturbation, darker shaded regions indicate a negative perturbation. Contour lines illustrate the base flow field as per figure 2.

on both vortices – compare with the profiles described by Lacaze *et al.* (2007) and Roy *et al.* (2008). As with the Crow instability, the perturbation field is dominant on the weaker vortex. Indeed, the amplitude of the perturbation mode shape acting on the stronger vortex is only $\simeq 6\,\%$ of that acting on the weaker vortex.

Over a very narrow range of ka, the Kelvin mode $[-1, 1, 1]$ is observed to be the dominant perturbation mode. A peak growth rate of $\sigma^* = 7.01$ is observed, at $\kappa_c = 1.64$. While the mode $[-1, 1, 1]$ is the mode with highest growth for $ka = [1.2, 1.5]$, the mode $[-2, 0, 1]$ also exhibits a significant growth rate in this range.

We therefore anticipate that both modes would be observed to compete experimentally at this wavenumber. However, the substantially higher growth rate of mode $[-2, 0, 1]$ (in the vicinity of $ka = [2.0, 3.0]$) should mean that this mode shape would dominate the overall perturbation into the nonlinear growth regime. Therefore, the mode competition would be difficult to isolate and identify, and should have little impact on the overall mode shape that the vortices exhibit. The mode shape for $[-1, 1, 1]$ is shown in figure 3(*d*). Once again, the perturbation field is dominant on the weaker vortex.

Comparing our findings with the results of Lacaze *et al.* (2007), we find that the value of κ_c varies considerably from that found for an equal-strength counter-rotating

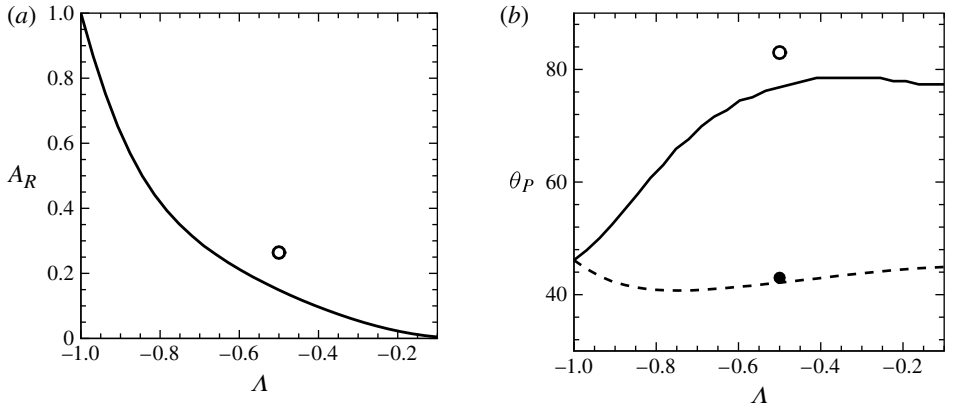

FIGURE 4. Vortex filament model predictions for the growth of the large-wavelength Crow instability. (*a*) The ratio of perturbation amplitude (A_R) acting on the strong vortex to the perturbation amplitude acting on the weak vortex, as a function of Λ. The circle indicates the amplitude ratio obtained from the linear stability calculations at $\Lambda = -0.5$. (*b*) The principal angle of the perturbation for the strong vortex (solid line) and the weak vortex (dashed line) as a function of Λ. The circles indicate the principal angles observed from the linear stability calculations at $\Lambda = -0.5$: the open circle corresponds to the strong vortex; the filled circle corresponds to the weak vortex.

Batchelor vortex pair. For mode $[-2, 0, 1]$, our finding of κ_c is 60 % higher than that found for a counter-rotating pair at $W^* = 0.3$ (Lacaze *et al.* 2007). By contrast, for mode $[-1, 1, 1]$, our finding of κ_c is 61 % less than that observed for a counter-rotating pair at $W^* = 0.15$. We note that Lacaze *et al.* (2007) did not report a growth of mode $[-1, 1, 1]$ at $W^* = 0.3$, nor a growth of mode $[-2, 0, 1]$ at $W^* = 0.15$.

Both Le Dizès & Laporte (2002) and Roy *et al.* (2008) compared the variation in κ_c for co- and counter-rotating equal-strength Lamb–Oseen vortex pairs. In general, they found that the co-rotating vortex pair exhibited a lower κ_c for all instability modes identified. This is ascribed to the global rotation rate inducing an additional Coriolis force on the system. In addition, Roy *et al.* (2008) considered the variation in κ_c for a co-rotating, equal-strength Batchelor vortex pair. Curiously, they found that κ_c for both modes $[-1, 1, 1]$ and $[-2, 0, 1]$ reduced when compared with the findings of Lacaze *et al.* (2007) for a counter-rotating Batchelor vortex pair.

While our vortex pair profile is substantially different from either investigation, the increase in κ_c for mode $[-2, 0, 1]$ reported here is surprising, and is worthy of future investigation.

Additionally, the rotation of the vortex pair was noted by Roy *et al.* (2008) to expand the range of ka over which significant growth of a mode was observed to occur, when compared to an equal-strength, counter-rotating pair. Figure 3(*a*) concurs with this finding.

Two other modes were identified (mode $[-2, 0, 2]$ and mode $[-3, -1, 1]$), both of which were predicted analytically by Lacaze *et al.* (2007). Neither mode had a significant growth rate, and it is not anticipated that they would have significant impact experimentally.

6.2.1. *Development of the Crow instability on unequal-strength vortex pairs*

A vortex filament model was employed to consider the Crow instability growing on an unequal-strength counter-rotating vortex pair. This extended the results from

the linear stability analysis from the case of $\Lambda = -0.5$ to the range $\Lambda = [-1, -0.1]$. The technique was precisely the same as that described by Bristol *et al.* (2004). The self-induction of each vortex core was calculated through solution of the dispersion equations provided by Saffman (1992).

The vortex filament model assumes that perturbations take the form of sinuous oscillations along the axis of each vortex. The model may be reduced to an eigenvalue problem, where the eigenvalues represent the global growth rate, and the eigenvectors represent the mode shape components. In particular, by taking the amplitude of the eigenvectors for each vortex, a ratio of 'perturbation strength' can be determined, measuring the relative strength of the perturbation on each vortex core. In addition, the plane of oscillation of the mode shape may be determined for each vortex, leading to the definition of a principal angle (θ_P). Here, the principal angle describes the angle that the mode shape makes with an imaginary line joining the vortex cores. Previous investigations have identified $|\theta_P| \simeq 45^\circ$ for $\Lambda = -1$.

The growth rates observed from the vortex filament model agree precisely with that reported by Bristol *et al.* (2004), with the growth rate increasing by $\simeq$28 % as Λ increases from -1 to -0.1. However, the ratio of perturbation amplitude acting on the stronger vortex with respect to the weaker vortex varies appreciably over this range (figure 4*a*). At $\Lambda = -0.5$, the stronger vortex is predicted to have a mode amplitude only 20 % that of the weaker vortex. The linear stability analysis study predicts a slightly higher ratio of 29 % at $\Lambda = -0.5$. The results shown in figure 4(*a*) would imply that the Crow instability will have relatively little impact on the development of the strong vortex for $|\Lambda| \lesssim 0.8$. This questions the efficacy of the Crow instability to enhance the dissipation of a generic vortex pair; the significant dissipation noted for $\Lambda = -1$ is an almost unique example where both vortices have substantial perturbation growth. This is despite the increase in the global growth rate of the mode as $\Lambda \to 0$.

In addition, the principal angle (θ_P) varies significantly for the stronger vortex as a function of Λ. Indeed, at $\Lambda = -0.5$, the vortex filament theory predicts $\theta_P \simeq 79^\circ$ for the stronger vortex, in agreement with the linear stability analysis model (as shown in figure 4*b*). As will be shown, this angle plays an important role in the nonlinear development phase.

As shown by Bristol *et al.* (2004), the rotation rate of the vortex pair plays a significant role in the perturbation growth of the Crow instability. Indeed, in the absence of rotation, the filament model predicts the growth of instabilities for both co- and counter-rotating vortex pairs. Following the analysis of Widnall *et al.* (1974) and Bristol *et al.* (2004), we now consider the equations governing a decoupled vortex filament pair, where the growth of instabilities on one vortex is not considered when determining the growth of instabilities on the neighbouring vortex. Using this approach, we can define

$$A_r = \Lambda \frac{\sin(2\theta_{P2})}{\sin(2\theta_{P1})}, \tag{6.5}$$

where θ_{P1} is the principal angle for the weaker vortex and θ_{P2} is the principal angle for the stronger vortex. We note that, should $|\theta_{P1}| = |\theta_{P2}| = 45^\circ$, A_R would reduce linearly with Λ. Comparing this with the findings in figure 4(*a*), the variation in either θ_{P1} and or θ_{P2} is to be anticipated.

For the decoupled system described, the principal angle for each vortex may be written as

$$\cos(2\theta_{P1}) = \Omega + \Lambda\varpi, \tag{6.6}$$

$$\cos(2\theta_{P2}) = \frac{1}{\Lambda}(\Omega + \varpi), \tag{6.7}$$

$$\Omega = \Lambda + 1, \tag{6.8}$$

where Ω is the normalized rotation rate of the vortex pair and ϖ is the self-induced angular velocity of a perturbation induced about the unperturbed axis of the vortex in question – see Saffman (1992) and Bristol *et al.* (2004) for further details. For the Crow instability, ϖ is a positive value, representing a retrograde rotation of the perturbations about the vortex. It is clear from (6.8) that the rotation rate of the vortex pair (Ω) plays a significant role in determining the principal angle of oscillation. In addition, we note that, given the retrograde nature of the Crow instability, a decoupled analysis predicts that no principal angle θ_{P2} satisfies (6.6) for $\Lambda = [-0.5, 0]$, and hence we would anticipate no growth on the stronger vortex for this range of Λ. Thus, the growth found on the stronger vortex in this range, for both the linear stability analysis study and the vortex filament study, must be induced by a direct coupling of instabilities growing on the weaker vortex.

We note that, for peak growth, $\theta_P = \pm 45°$. For the stronger vortex, owing to the retrograde motion of the perturbation, this is not possible except for the unique case of $\Lambda = -1$. Considering (6.7), we anticipate that $\theta_P > \pm 45°$, for all cases except for $\Lambda = -1$, in agreement with the findings of the coupled filament model (figure 4*b*).

For the weaker vortex, $\theta_P = \pm 45°$ may occur for all values of $\Lambda = [-1, 0]$, and we surmise that it is for this reason that the coupled filament analysis technique shows that θ_{P1} remains near 45° for all values of Λ, resulting in peak instability growth on the weaker vortex.

6.3. *Direct numerical simulation results*

6.3.1. *Two-dimensional evolution of the vortex pair*

The initial profile of the vortex pair for the DNS simulations has been described in § 2. Relaxation of the vortex pair was determined in full three-dimensional space, and was noted to agree precisely with that found in § 6.1. Relaxation of the vortex pair was deemed to be complete at $t^*_{nv} = 30$, corresponding to $t^* = 0.47$. At this time, the vortex pair exhibited the same characteristics as previously described in § 6.1 and presented in table 1. Relaxation was concluded prior to perturbation growth being recorded in any higher modes.

6.3.2. *Perturbation growth on the vortex pair*

Figure 5 shows the development of the instability as a function of time. Here, we visualize the flow field by employing the λ_2 field, defined as the second eigenvalue solution to the tensor $\boldsymbol{S}^2 + \boldsymbol{\Omega}^2$ (Jeong & Hussain 1995). Here, $\boldsymbol{S}$ is the symmetric component of the velocity gradient tensor ($\boldsymbol{\nabla u}$), and $\boldsymbol{\Omega}$ is its antisymmetric component. A vortex core is defined to exist where $\lambda_2 < 0$, and the extremity of the vortex core is described by the contour $\lambda_2 = 0$. Figure 5(*a*) shows a snapshot at $t^* = 1.56$, corresponding to a time soon after the transition from linear to nonlinear growth of the perturbation field. The helical structure of the instability mode growing on the weaker vortex is typical of mode $[-2, 0]$. No perturbations are visible on the stronger vortex. Figure 5(*b–d*) shows snapshots during the nonlinear development of the perturbation. From $t^* = 1.81$, vortex filaments are observed to emanate from the weaker vortex; at later times these wrap around the stronger vortex core ($t^* \gtrsim 2.07$). At $t^* = 2.34$ (the final time shown in figure 5), the weak vortex has broken up into a series of discrete vortex filaments, each wrapped around the stronger vortex. The looping structures cause periodic stretching of the stronger vortex, generating periodic

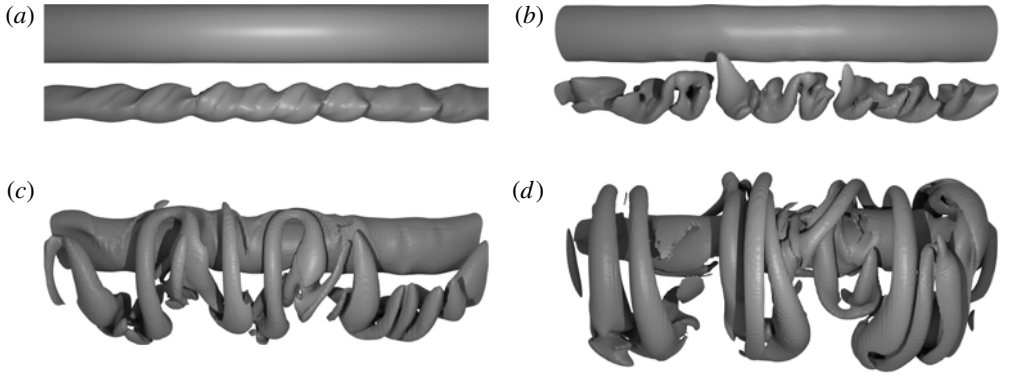

FIGURE 5. Snapshots showing iso-surface contours of the λ_2 field during nonlinear development of the instability (taken from DNS): (*a*) $t^* = 1.56$; (*b*) $t^* = 1.81$; (*c*) $t^* = 2.07$; and (*d*) $t^* = 2.34$. In each case, the iso-surface contour level chosen is $\lambda_2 = -0.1$.

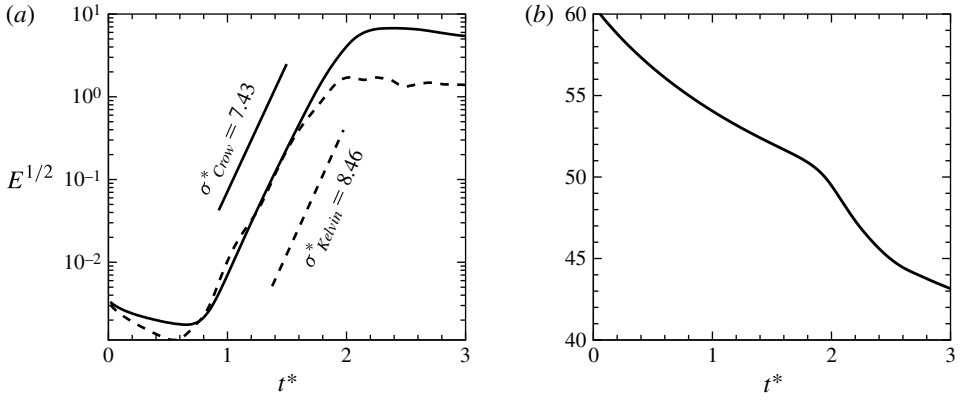

FIGURE 6. The square root of the total kinetic energy by mode as a function of t^*. (*a*) Plot of $E^{1/2}$ for mode 3 corresponding to the Crow instability (solid line) and mode 8 corresponding to the Kelvin mode $[-2, 0, 1]$ instability (dashed line). The gradient of these lines provides the growth rate of the instability modes, and measurements are indicated through the linear growth phase. (*b*) The reduction in $E^{1/2}$ for the fundamental mode; the transition to nonlinear growth is apparent at the point where the gradient changes discontinuously.

undulations of the stronger vortex profile ($t^* = 2.34$), with a period commensurate with the Crow instability wavelength. However, the perturbations are relatively small and the stronger vortex retains its coherence until the conclusion of the simulation.

Following the work of Laporte & Corjon (2000), the square root of the kinetic energy ($E^{1/2}$), measured for each Fourier mode, was used to directly predict the growth rate of perturbations. Figure 6(*a*) shows $E^{1/2}$ for mode $m = 3$ (representing the growth of the Crow instability) and mode $m = 8$ (representing the growth of the Kelvin mode $[-2, 0, 1]$). These were the modes identified as displaying most energy using the stability analysis technique. Correspondingly, they were the modes that exhibited the highest energy during the linear phase of growth in the DNS investigation.

Linear growth of the short-wavelength mode commences at $t^* \simeq 0.55$, with a growth rate of $\sigma^* = 8.46$ being observed – in close agreement with the linear stability analysis

($\sigma^* = 8.5$). Linear growth concludes at $t^* \simeq 1.5$ where nonlinear terms begin to dominate, reducing the growth rate in agreement with theory presented by Eloy & Le Dizès (1999).

The Crow instability commences linear growth at a later time, $t^* \simeq 0.65$. Its linear growth rate is smaller than the Kelvin mode with $\sigma^* = 7.43$ (in close agreement with the linear stability analysis where $\sigma^* = 8.67$). Linear growth of the Crow instability concludes at $t^* \simeq 2.00$. We note that the growth rate of the Crow instability becomes nonlinear at a later stage than the Kelvin mode. This may be directly linked to the larger wavelength of the Crow instability. Small-scale structures, evolving in the nonlinear growth phase, have less impact on the large-wavelength Crow instability when compared to the comparatively short-wavelength Kelvin mode.

The growth rates predicted from the DNS, during the linear growth regime, were found to be very close to those predicted by linear stability analysis, verifying the applicability of the linear stability analysis technique employed. During the linear growth phase, the decrease in growth rate of the Kelvin mode, observed in the DNS calculations, is due to vortex core radii growth as a function of time, as described in § 4.3.

Figure 6(*b*) shows $E^{1/2}$ for the zeroth (two-dimensional) mode; $E^{1/2}_{k=0}$ is noted to decay as a function of time during the linear phase of growth. An abrupt decrease in $E^{1/2}_{k=0}$ is observed as the Crow instability transitions from linear to nonlinear growth, as energy is transferred away from the $E_{k=0}$ mode to higher modes. At the conclusion of the simulation ($t^* = 3.00$), $E^{1/2}_{k=0}$ is $\simeq$10 % less than what would be anticipated through the action of dissipative forces alone. From observation of figure 5, we note that much of this energy transfer happens within the weaker vortex.

6.3.3. *Perturbation mode shapes: direct numerical simulation results*

Perturbation fields at each critical wavenumber were obtained by extracting the Fourier mode from the calculated DNS flow field corresponding to the instability mode of interest. This allows the resultant instability mode shapes to be compared directly with the results from the linear stability study.

Two wavenumbers are considered here, corresponding to $ka = 1.5$ (where mode $[-1, 1, 1]$ and mode $[-2, 0, 1]$ were predicted to compete) and $ka = 2.5$ (where mode $[-2, 0, 1]$ was predicted to dominate). While not shown here, the relatively simpler mode shape corresponding to the Crow instability was found to agree precisely with that predicted by the linear stability analysis technique.

Figure 7(*a*) shows an arbitrarily chosen x–y slice of the perturbation field for $ka = 1.5$ at $t^* = 1.2$. The twisting nature of mode $[-2, 0, 1]$ means that the mode shape varies significantly along the axis of the vortex. The axial position of the x–y slice has been chosen to agree closely with the mode shapes shown in figure 3. The mode shape acting on the weaker vortex is clearly dominated by mode $[-2, 0, 1]$. By contrast, on the stronger vortex, the mode shape, while strictly being defined as a mode $[-2, 0, 1]$ profile, bears striking similarities to mode $[-1, 1, 1]$ shown in figure 3(*d*).

During the linear growth phase, the mode shapes are well described as $T2$-periodic along the axial direction. That is, the perturbation structures are identical half a perturbation wavelength along the axis, except that the sign of the perturbation is reversed. For this reason, we also consider the perturbation field for $ka = 1.5$ a quarter of a wavelength away from that shown in figure 7(*a*) (shown in figure 7*b*). At this cross-section, the mode shape corresponds to mode $[-2, 0, 1]$ on both vortices.

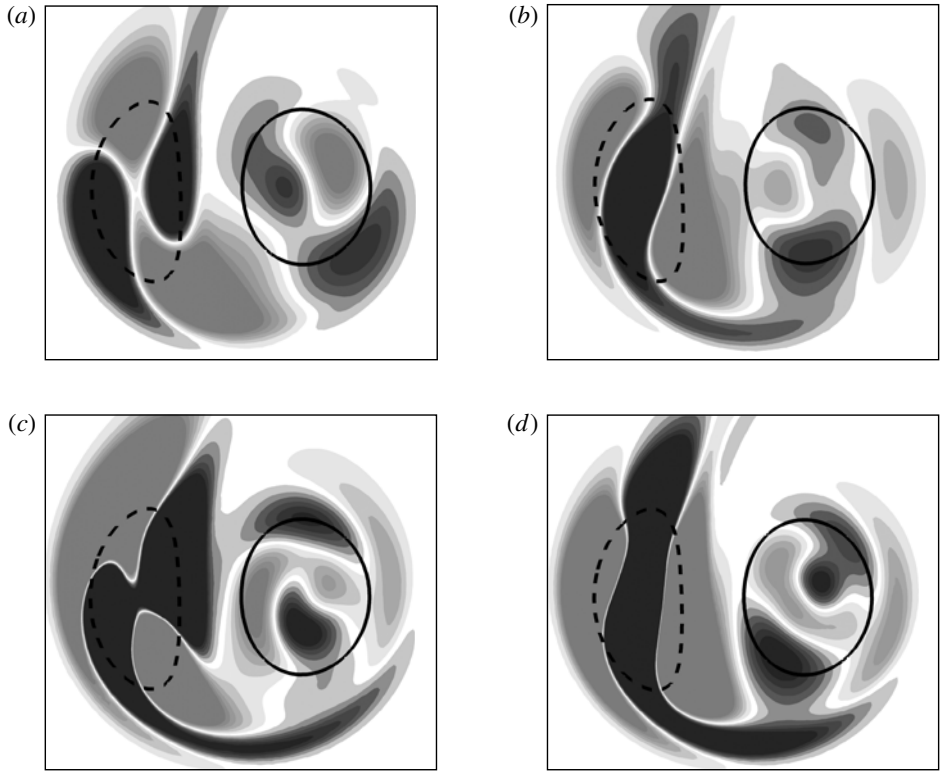

FIGURE 7. Perturbation axial vorticity fields obtained from DNS investigation. Fields are obtained by extracting Fourier modes of interest from the total solution. The panels show slices of these fields taken along the z axis. Slice locations have been chosen to compare directly with the findings from the linear stability study (figure 3). (*a*) The perturbation field for mode 5. (*b*) The same mode as (*a*), but the slice is taken one quarter of a wavelength further along the z axis. (*c*) The perturbation field for mode 8. (*d*) The same mode as (*c*), but the slice is taken one quarter of a wavelength further along the z axis. In each case, shaded contours are of the perturbation field; lightly shaded regions indicate a positive perturbation, and darker shaded regions indicate a negative perturbation. Line contours illustrate the base flow field as per figure 2.

Figure 7(*c*,*d*) shows arbitrarily chosen x–y slices of the perturbation field for $ka = 2.5$ at $t^* = 1.2$. In this case, the perturbation mode shape growing on both vortices is in agreement with that predicted for mode $[-2, 0, 1]$. In particular, the mode shape shown in figure 7(*c*) is nearly identical to that predicted by the linear stability analysis (figure 3*c*).

6.4. *Nonlinear development – stage 1*

Given that the weaker vortex displays significantly more deformation through the nonlinear growth phase, we now consider the nonlinear perturbations growing on it in isolation. Nonlinear development of the vortex pair occurs over two distinct stages. In the first stage, the weaker vortex evolves to form axially periodic 'clumps' of vorticity with a wavelength commensurate with the Kelvin perturbation. The second stage is distinguished by the development of azimuthal filaments of vorticity emanating from the weaker vortex; these evolve to wrap around the stronger vortex.

A number of approaches exist to define the profile of a vortex core in a three-dimensional domain, principal among which is the λ_2 field. Several prior investigations have considered the magnitude of vorticity ($|\boldsymbol{\omega}|$) as a definition of the vortex core profile (see e.g. Laporte & Corjon 2000; Bristol *et al.* 2004), while others have considered the axial component of vorticity in isolation (Leweke & Williamson 1998). As will be shown, we note a significant difference in the profile of the vortex core as defined by the λ_2 field when compared to the magnitude of vorticity ($|\boldsymbol{\omega}|$). This may result in significant differences in vortex profile when comparing experimental visualizations to DNS investigations, which have predominantly considered $|\boldsymbol{\omega}|$. In order to investigate the cause of this discrepancy, it is advantageous to simplify the equations that define the λ_2 field, such that the dominant processes underpinning the initial stages of nonlinear development may be clearly elucidated.

The definition of the λ_2 field can be rewritten in a significantly simpler form by the assumption that the rate of change of all velocity components in the axial direction is less pronounced than that in the x–y plane. This assumption is valid for two reasons: first, the base flow field has no variation in the axial direction; second, the perturbation velocity components vary more abruptly in the x–y plane than in the axial direction. We assume that this same approximation holds during the initial stages of the nonlinear growth regime. Hence we may write

$$\omega_{xz} \simeq \tau_{xz} \simeq \frac{\partial w}{\partial x}, \tag{6.9}$$

$$\omega_{yz} \simeq \tau_{yz} \simeq \frac{\partial w}{\partial y}, \tag{6.10}$$

$$\tau_{zz} \simeq 0. \tag{6.11}$$

With these assumptions, the antisymmetric component of the velocity gradient tensor simplifies to

$$\boldsymbol{\Omega} \simeq \begin{bmatrix} 0 & \omega_{xy} & \dfrac{\partial w}{\partial x} \\ -\omega_{xy} & 0 & \dfrac{\partial w}{\partial y} \\ -\dfrac{\partial w}{\partial x} & -\dfrac{\partial w}{\partial y} & 0 \end{bmatrix}, \tag{6.12}$$

and the symmetric component of the velocity gradient tensor to

$$\boldsymbol{S} \simeq \begin{bmatrix} \tau_{xx} & \tau_{xy} & \dfrac{\partial w}{\partial x} \\ \tau_{xy} & \tau_{yy} & \dfrac{\partial w}{\partial y} \\ \dfrac{\partial w}{\partial x} & \dfrac{\partial w}{\partial y} & 0 \end{bmatrix}. \tag{6.13}$$

From these definitions, and in the vicinity of the weaker vortex, we may approximate the equation defining the eigenvalues (λ) as

$$\begin{aligned} &(-\omega_{xy}^2 + \tau_{xx}^2 + \tau_{xy}^2 - \lambda)^2 \lambda + \alpha^2(-\omega_{xy}^2 + \tau_{xx}^2 + \tau_{xy}^2 - \lambda) \\ &\quad + \beta^2(-\omega_{xy}^2 + \tau_{xx}^2 + \tau_{xy}^2 - \lambda) = 0, \end{aligned} \tag{6.14}$$

$$\alpha = \omega_{xy}\frac{\partial w}{\partial y} + \tau_{xx}\frac{\partial w}{\partial x} + \tau_{xy}\frac{\partial w}{\partial y}, \tag{6.15}$$

$$\beta = -\omega_{xy}\frac{\partial w}{\partial x} + \tau_{yy}\frac{\partial w}{\partial y} + \tau_{xy}\frac{\partial w}{\partial x}. \tag{6.16}$$

The development of (6.14)–(6.16) relies on the assumption that $\tau_{zz} \simeq 0$. This allows us to write that, owing to continuity, $\tau_{xx} \simeq -\tau_{yy}$. Inspection of (6.14) reveals that the component defining λ_2 (the second largest root of (6.14)) may be written as

$$\lambda_{2_\varepsilon} = -\omega_{xy}^2 - \tau_{xx}\tau_{yy} + \tau_{xy}^2 = \frac{\partial v}{\partial x}\frac{\partial u}{\partial y} - \frac{\partial u}{\partial x}\frac{\partial v}{\partial y}. \tag{6.17}$$

Here we have defined λ_{2_ε} (our simplified approximation) to differentiate this from an exact calculation of the λ_2 field. Perhaps unsurprisingly, it is the component of strain in the x–y plane, coupled with ω_{xy}, that acts to dominate the definition of the λ_2 field. Herein we define

$$\tau_D = \tau_{xy}^2 - \tau_{xx}\tau_{yy} \tag{6.18}$$

as the 'dominant strain'. Should the magnitude of the dominant strain exceed that of ω_{xy}^2, then the local fluid environment is dominated by the strain field, and the λ_{2_ε} field will not identify a vortex core at this location.

We note in passing that the approximation for λ_2 defined by (6.17) is equally valid for the case of a Lamb–Oseen vortex pair. However, in that case, we may also assume that the axial component of velocity is small relative to the other components, simplifying (6.14).

Figure 8 shows three definitions predicting the profile of the weaker vortex core for $t^* = 1.57$ (figure 8*a–c*) and $t^* = 1.66$ (figure 8*d–f*). Iso-surfaces of the λ_{2_ε} field are shown in figures 8(*a*) and 8(*d*); iso-surfaces of the λ_2 field are shown in figures 8(*b*) and 8(*e*); and iso-surfaces of $|\boldsymbol{\omega}|$ are shown in figures 8(*c*) and 8(*f*). The values of λ_2, λ_{2_ε} and $|\boldsymbol{\omega}|$ have been carefully chosen to ensure that the profiles agree in areas where the strain rate approaches zero. In each case, the strong vortex (not shown) is to the right-hand side of the weaker vortex. It is clear that the λ_2 field identifies a vortex core profile that is markedly different from that identified by considering $|\boldsymbol{\omega}|$. At both times, the iso-surfaces of λ_{2_ε} correctly identify the major structures of the λ_2 iso-surface.

Importantly, localized regions of tapering on the right-hand side of the vortex core profile (identified by both λ_2 and λ_{2_ε}) are not observed when considering the $|\boldsymbol{\omega}|$ field. Indeed, these regions correspond closely to a localized thickening of the vortex core profile, as predicted by the $|\boldsymbol{\omega}|$ field. Figure 8 also identifies that the region of highest dominant strain rate corresponds almost precisely with the location of localized tapering, in agreement with (6.17). On the left-hand side of the vortex, the profiles described by both λ_2 and $|\boldsymbol{\omega}|$ agree very closely. We note that the dominant strain rate is negligible on the left-hand side of the vortex core. The effect of the dominant strain is to cause the Λ_2 field to develop out of phase with $|\boldsymbol{\omega}|$ along the axis of the weaker vortex.

The dominant strain rate varies along the axis of the vortex with a period commensurate with the $[-2, 0, 1]$ mode. Indeed, the periodic variation in λ_2 is due purely to the nonlinear development of the $[-2, 0, 1]$ mode. We can show this by isolating the Fourier mode corresponding to the mode $[-2, 0, 1]$ ($ka = 2.5$ in this case). Figure 9 shows cross-sections of the perturbation dominant strain rate for $t^* = 1.00$ (well within the linear growth regime) and $t^* = 1.66$ (well within the nonlinear growth regime). The profiles of the two fields are essentially identical. While not shown,

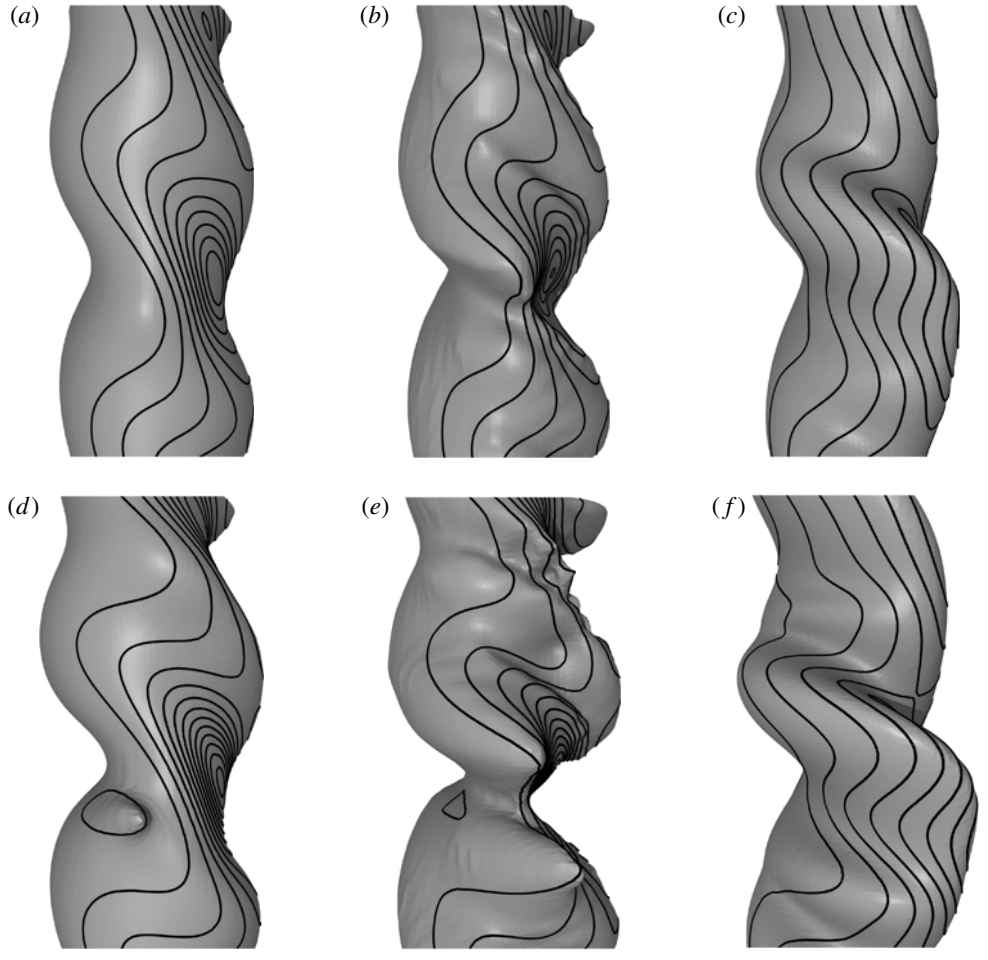

FIGURE 8. Snapshots of iso-surface contours of the weaker vortex showing the development of the perturbation in the first stage of nonlinear growth: (*a–c*) the weaker vortex at $t^* = 1.58$; (*d–f*) the weaker vortex captured at $t^* = 1.66$; (*a*,*d*) iso-surfaces of $\lambda_{2_\varepsilon} = -0.1$; (*b*,*e*) iso-surfaces of $\lambda_2 = -0.1$; and (*c*,*f*) iso-surfaces of $|\boldsymbol{\omega}| = 1.75$ (chosen such that regions of low strain rate would agree across all iso-surfaces). The iso-surfaces are overlaid with contour lines of the dominant strain, τ_D, with $\Delta\tau_D = 1$. In each case, the peak dominant strain is on the right-hand side of the iso-surface.

the perturbation ω_{xy} field is also nearly identical in structure when comparing both time steps. This leads us to the conclusion that the first stage of nonlinear growth is due solely to the progression of the linear mode. No new mechanism causes the variation in vortex core profiles observed during this phase of development. Instead, the $[-2, 0, 1]$ mode grows sufficiently such that it significantly alters the base flow field.

Beyond $t^* \simeq 1.7$ further distortion of the weak vortex is due to a different mechanism. This new mechanism results in the formation of periodically spaced azimuthal vortex tubes along the axis of the weak vortex core (figure 5). Similar vortex tubes have been described by Thomas & Auerbach (1994) and Laporte & Corjon (2000), and are referred to as secondary vortices by Leweke & Williamson

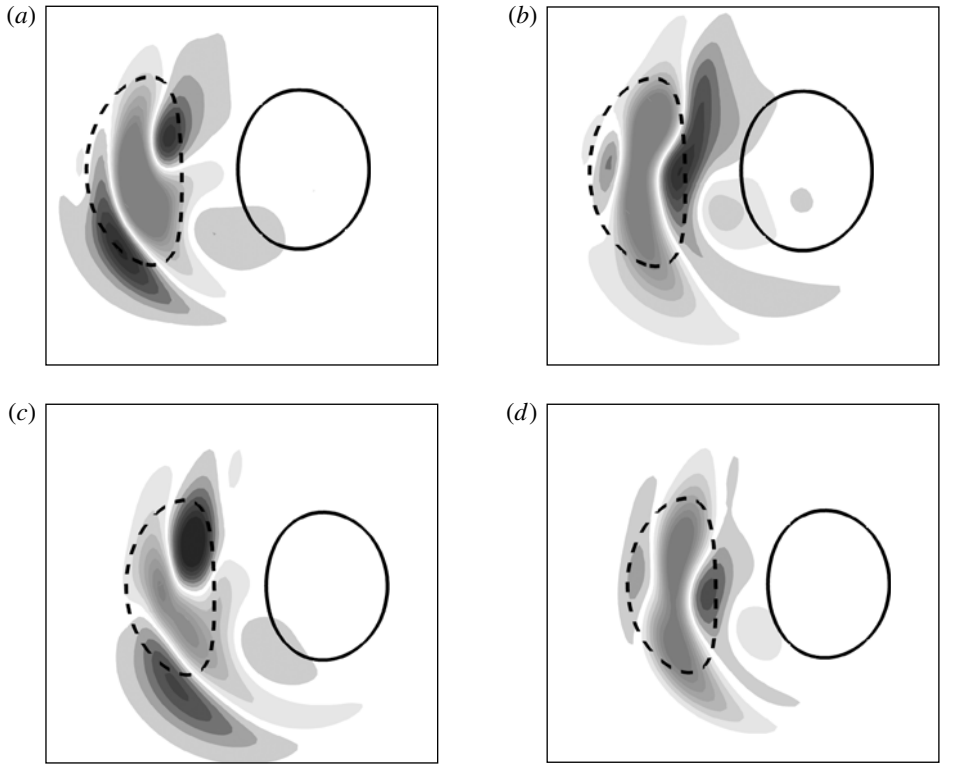

FIGURE 9. Perturbation dominant strain fields obtained from DNS investigation. Fields are obtained by extracting the eighth Fourier mode (corresponding to the Kelvin mode $[-2, 0, 1]$) from the total solution. Images show slices of these fields taken along the z axis: (a,b) at $t^* = 1.00$ (well within the linear growth phase); (c,d) at $t^* = 1.66$ (well within the nonlinear growth phase); (b) and (d) are taken one quarter of a wavelength away from (a) and (c), respectively. In each case, shaded contours are of the perturbation field; lightly shaded regions indicate a positive perturbation, and darker shaded regions indicate a negative perturbation. Line contours illustrate the base flow field as per figure 2.

(1998) for the case of equal-strength Lamb–Oseen vortices. Owing to the change in dominant driving mechanism, we refer to $t^* \simeq 1.7$ as the transitional time.

6.5. *Nonlinear development – stage 2: the generation of secondary vortices*

Figure 10 shows the progression of the weaker vortex core through the second stage of the nonlinear growth regime. Iso-surfaces of $\lambda_2 = -0.1$ are shown in figure 10(a–c), while iso-surfaces of $|\boldsymbol{\omega}| = 1.75$ are shown in figure 10(d–f).

Considering the $|\boldsymbol{\omega}|$ field, we note that there are two distinct bulges, which are drawn azimuthally to the right-hand side of the weaker vortex core (and hence drawn towards the stronger vortex). These azimuthal bulges are noted to occur at a frequency commensurate with the short-wavelength instability, and are referred to herein as secondary vortices.

The location of peak λ_2, along the axis of the weak vortex, at the conclusion of the initial stage of nonlinear growth induces two arms of λ_2 to emanate from the weaker vortex core at every position where $|\boldsymbol{\omega}|$ exhibits an azimuthal bulge (and crosses the critical streamline).

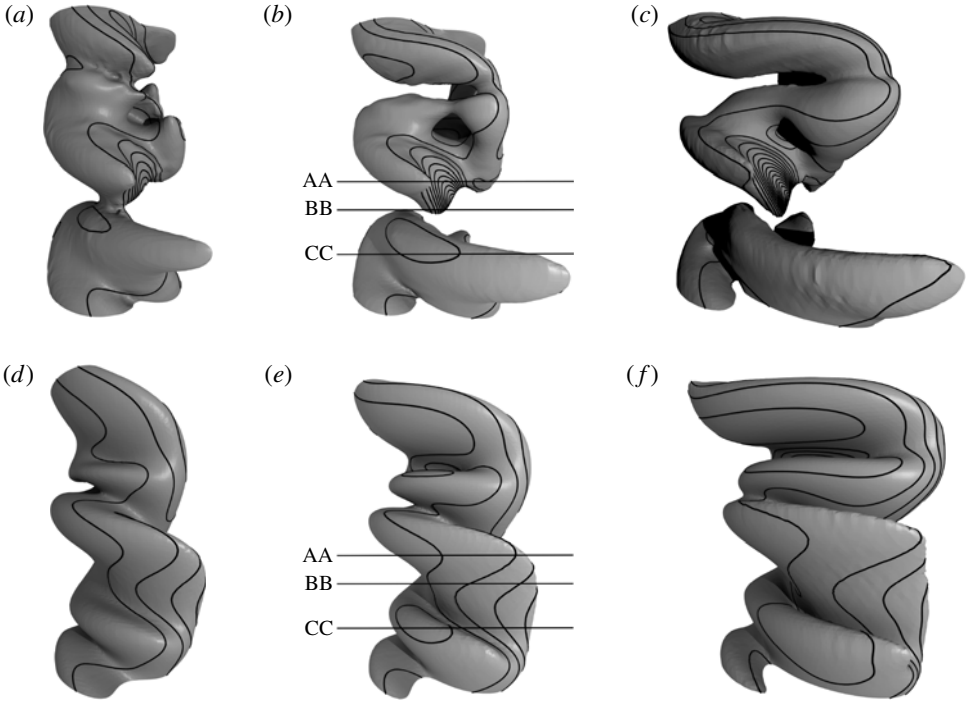

FIGURE 10. Snapshots of iso-surface contours showing the development of the perturbation in the second stage of nonlinear growth: (*a–c*) the weak vortex using iso-contours of $\lambda_2 = -0.1$; (*d–f*) the weak vortex using iso-contours of $|\boldsymbol{\omega}| = 1.75$; (*a*,*d*) $t^* = 1.71$; (*b*,*e*) $t^* = 1.79$; (*c*,*f*) $t^* = 1.87$. The iso-surfaces are overlaid with contour lines of the dominant strain, τ_D, with $\Delta\tau_D = 2$. In each case, the peak dominant strain is on the right-hand side of the iso-surface.

Observation of the x–y streamlines, calculated in a reference frame fixed to the moving vortex pair, reveals the mechanism driving the formation of the secondary vortices. Figure 11 shows, at a range of axial locations, contours of ω_{xy} with streamlines overlaid. At each axial location, the streamlines form hyperbolic points located upstream and downstream of the vortex pair. The streamline joining the two hyperbolic points is referred to as the critical streamline. Any vorticity crossing the critical streamline will be convected azimuthally around the neighbouring (stronger) vortex.

This phenomenon is well known; in two-dimensional flows, it leads to vortex stripping (see e.g. Mariotti, Legras & Dritschel 1994), significantly altering the progression of the vortex pair. In three-dimensional flows, the vorticity crosses the critical streamline periodically at the same axial wavelength as the Kelvin mode. Where the Crow instability draws one vortex closer to its neighbour, the effect is heightened, as a greater magnitude of vorticity crosses the critical streamline.

In figure 11(*b*), a proportion of the ω_{xy} field, emanating from the weaker vortex, has crossed the critical streamline. At later times, this region of vorticity continues to be pulled away from the weaker vortex core position, around the stronger vortex. Cross-sections taken immediately above (figure 11*a*) and below (figure 11*c*) the azimuthal bulge have less vorticity crossing the critical streamline. We observe that the slice shown in figure 11(*b*) has a local minimum in λ_2; local maxima are observed

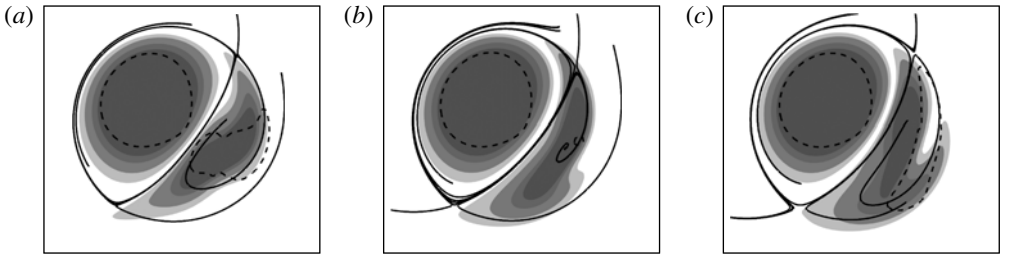

FIGURE 11. Cross-sections of vortex core development at $t^* = 1.79$: (*a*), (*b*) and (*c*) correspond to sections AA, BB and CC, respectively, in figure 10. Shaded contours are of ω_{xy}; dashed lines are $\lambda_2 = -0.1$; and thin continuous lines are streamlines calculated in the reference frame attached to the rotating vortex pair.

immediately above and below this slice, leading to two arms of λ_2 to be formed for each Kelvin mode wavelength.

Our observations of the progression of the λ_2 field are in close agreement with the experimental observations of Leweke & Williamson (1998). They noted two secondary vortex filaments occurring per short-wavelength instability for a counter-rotating, equal-strength Lamb–Oseen vortex pair. While the Kelvin mode $[-1, 1, 1]$ (observed on the Lamb–Oseen vortex pair) is substantially different in profile to the $[-2, 0, 1]$ mode observed here, we predict that the strain field would induce similar effects on the progression of the Lamb–Oseen vortex pair to that described in § 6.4.

6.6. *Late-stage nonlinear development*

Figure 12 shows the late-stage development of the vortex pair ($t^* = 1.87$ to $t^* = 2.21$). Both λ_2 and the magnitude of vorticity ($|\boldsymbol{\omega}|$) are employed to identify the vortex core. The process described in § 6.5 has continued, pulling filaments from the weaker vortex completely around the stronger vortex. At these later stages, the Crow instability dominates the advection of the weaker vortex, leading to three distinct locations where the weaker vortex has been sheared around the stronger vortex. The smaller-scale Kelvin mode structures are still present, but they are only significant at three distinct locations in the axial direction.

It is interesting to note that, at this late stage of development, the peak magnitude of vorticity is contained within the azimuthal filaments emanating from the weaker vortex (not within the stronger vortex); the increased strength in vorticity is due to the conservation of momentum as the azimuthal filaments are stretched around the stronger vortex.

In addition, we observe that the vorticity profile predicted by the $|\boldsymbol{\omega}|$ field approaches that predicted by λ_2 as a function of time. Indeed, at $t^* = 2.2$, only minor variations are observed between the two definitions. This convergence of vortex core profile definitions is due to the late-stage evolution of the weaker vortex core as filaments of azimuthal vorticity are stretched around the stronger vortex. We note that, within each vortex filament, the maximum vorticity component acts in the azimuthal direction (relative to the stronger vortex), parallel to the direction of principal strain. For this reason, $\lambda_2 \simeq |\boldsymbol{\omega}|$, and the two definitions converge. This is in sharp contrast to the early stages of nonlinear development, where the direction of maximum vorticity was normal to the direction of principal shear (as discussed in § 6.4).

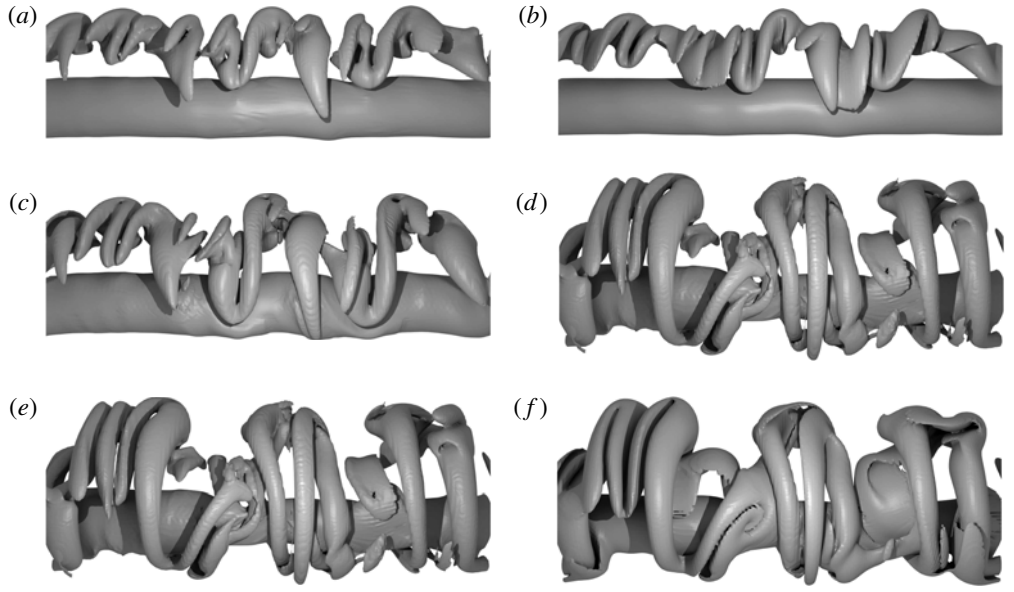

FIGURE 12. Snapshots of iso-surface contours showing the late-stage development of the perturbation: the vortex pair is captured at (*a*,*b*) $t^* = 1.87$, (*c*,*d*) $t^* = 2.00$ and (*e*,*f*) $t^* = 2.21$; (*a*,*c*,*e*) iso-contours of $\lambda_2 = -0.1$; (*b*,*d*,*f*) iso-contours of $|\boldsymbol{\omega}| = 1.75$. This iso-contour level of $|\boldsymbol{\omega}|$ has been chosen such that the profile of the stronger vortex appears identical to that predicted by $\lambda_2 = -0.1$.

7. Discussion

Overall, our findings question the efficacy of Crow and Kelvin instability modes to enhance the dissipation of the vortex pair system for $|\Lambda| \neq 1$. Our choice of W^* was crucial in selecting which elliptic modes would dominate – a different selection would have promoted other modes to grow in preference. However, considering the work of both Lacaze *et al.* (2007) and Roy *et al.* (2008), modes $[-1, 1, 1]$, and $[-2, 0, 1]$ dominate other modes for a considerable range of W^* for both co- and counter-rotating vortex pairs of equal circulation strength magnitude. We also note that the choice of a/b (and hence ε_{ext}) has a direct effect on the growth rate of any of the instabilities discussed.

Our detailed investigation of $\Lambda = -0.5$ clearly shows that, while the weaker vortex undergoes significant twisting and stretching, the stronger vortex exhibits virtually no variation in its structure, in general agreement with the finding for an unequal-strength Lamb–Oseen vortex pair (see e.g. Bristol *et al.* 2004). There are two causes for this: first, the strain induced on the stronger vortex is significantly weaker, resulting in lower-amplitude perturbation mode shapes in the vicinity of the stronger vortex; second, the reduction in strain on the stronger vortex alters the principal angle of the Crow instability acting on the stronger vortex. In the case of $\Lambda = -1$, the principal angle drives the perturbed vorticity towards the critical streamline, allowing the neighbouring vortex to further stretch the perturbed vorticity filaments in the nonlinear phase of growth. However, as θ_p increases, the (weakly) perturbed vortex elements of the strong vortex are no longer driven towards the critical streamline, reducing instability growth in the nonlinear phase.

The global rotation of the vortex pair induces high growth over a wider range of ka than found for an equal-strength counter-rotating vortex pair, in agreement with prior studies.

As predicted by Lacaze *et al.* (2007), it is the $[-2, 0]$ Kelvin mode that grows preferentially to the $[-1, 1]$ mode observed for Lamb–Oseen vortex pairs. As the Batchelor vortex represents the asymptotic solution for a trailing line vortex profile far downstream of an aircraft, it is unlikely that the mode $[-1, 1]$ would be observed in an aircraft wake. Indeed, from the theoretical predictions presented by Lacaze *et al.* (2007), this will only occur for very low values of W^*. However, regardless of which short-wavelength instability mode dominates, it is the advection of vorticity elements across the critical streamline that provides the most dramatic dissipation of a vortex core. Successful use of such passive dissipation techniques relies on the linear mode shape to actively propel vortex elements in this manner.

8. Conclusions

The combination of a linear stability analysis study with a three-dimensional direct numerical simulation has allowed us to determine the evolution of instabilities in an unequal-strength counter-rotating Batchelor vortex pair through both the linear and nonlinear growth regimes.

As shown by Lacaze *et al.* (2007), Batchelor vortex pairs exhibit a range of Kelvin mode shapes beyond those found for Lamb–Oseen vortex pairs. Our findings support their conclusions: a Kelvin mode $[-2, 0]$ is observed to grow in preference to the Kelvin mode $[-1, 1]$ in the linear growth phase, and this alters the progression of the nonlinear development, especially in the initial and secondary stages of nonlinear development. Tertiary nonlinear development is dominated by the Crow instability. The mode shape and growth rate of the Crow instability is nearly identical to that expected for a Lamb–Oseen vortex pair, and thus the final mode shape of the vortex pair appears similar to prior DNS investigations of a Lamb–Oseen vortex pair.

Instability growth occurs predominantly on the weaker vortex, leading to secondary vortex filaments wrapping around the stronger vortex. It is only in the tertiary stage of nonlinear growth that perturbations are observed to grow on the stronger vortex.

Acknowledgements

The authors thank the Monash eResearch Centre (MeRC) for access to their central compute facility. C.J.B. thanks Monash Engineering for the Engineering Research Allowance supporting his study. G.J.S. thanks NCI for access to their National Facility through a Merit Allocation Scheme grant. NCI is supported by the Australian Commonwealth Government. K.R. and G.J.S. received financial support from Monash University Faculty of Engineering Small Grants.

REFERENCES

ASH, R. L. & KHORRAMI, M. R. 1995 Vortex stability. In *Fluid Vortices* (ed. S. I. Green), chap. 8, pp. 317–372. Kluwer.

BATCHELOR, G. K. 1964 Axial flow in trailing line vortices. *J. Fluid Mech.* **20** (4), 645–658.

BLACKBURN, H. M. & SHEARD, G. J. 2010 On quasi-periodic and subharmonic Floquet wake instabilities. *Phys. Fluids* **22** (3), 031701.

BLACKBURN, H. M. & SHERWIN, S. J. 2004 Formulation of a Galerkin spectral element–Fourier method for three-dimensional incompressible flows in cylindrical geometries. *J. Comput. Phys.* **197** (2), 759–778.

BRISTOL, R. L., ORTEGA, J. M., MARCUS, P. S. & SAVAŞ, Ö. 2004 On cooperative instabilities of parallel vortex pairs. *J. Fluid Mech.* **517**, 331–358.

CROUCH, J. D. 1997 Instability and transient growth for two trailing-vortex pairs. *J. Fluid Mech.* **350**, 311–330.

CROW, S. C. 1970 Stability theory for a pair of trailing vortices. *AIAA J.* **8** (12), 2172–2179.

ELOY, C. & LE DIZÈS, S. 1999 Three-dimensional instability of Burgers and Lamb–Oseen vortices in a strain field. *J. Fluid Mech.* **378**, 145–166.

FABRE, D., JACQUIN, L. & LOOF, A. 2002 Optimal perturbations in a four-vortex aircraft wake in counter-rotating configuration. *J. Fluid Mech.* **451**, 319–328.

GARTEN, J. F., WERNE, J., FRITTS, D. C. & ARENDT, S. 2001 Direct numerical simulations of the Crow instability and subsequent vortex reconnection in a stratified flow. *J. Fluid Mech.* **426**, 1–45.

HEATON, C. J. 2007 Centre modes in inviscid swirling flows, and their application to the stability of the Batchelor vortex. *J. Fluid Mech.* **576**, 325–348.

JEONG, J. & HUSSAIN, F. 1995 On the identification of a vortex. *J. Fluid Mech.* **285**, 69–94.

JIMENEZ, J. 1975 Stability of a pair of corotating vortices. *Phys. Fluids* **18**, 1580–1581.

KARNIADAKIS, G. E., ISRAELI, M. & ORSZAG, S. A. 1991 High-order splitting methods for the incompressible Navier–Stokes equations. *J. Comput. Phys.* **97** (2), 414–443.

KARNIADAKIS, G. E. & SHERWIN, S. J. 2005 *Spectral/hp Element Methods for Computational Fluid Dynamics*, 2nd edn. Oxford University Press.

KARNIADAKIS, G. E. & TRIANTAFYLLOU, G. S. 1992 Three-dimensional dynamics and transition to turbulence in the wake of bluff objects. *J. Fluid Mech.* **238**, 1–30.

KERSWELL, R. R. 2002 Elliptical instability. *Annu. Rev. Fluid Mech.* **34**, 83–113.

LACAZE, L., BIRBAUD, A.-L. & LE DIZÈS, S. 2005 Elliptic instability in a Rankine vortex with axial flow. *Phys. Fluids* **17**, 017101–1.

LACAZE, L., RYAN, K. & LE DIZÈS, S. 2007 Elliptic instability in a strained Batchelor vortex. *J. Fluid Mech.* **577**, 341–361.

LAPORTE, F. & CORJON, A. 2000 Direct numerical simulations of the elliptic instability of a vortex pair. *Phys. Fluids* **12**, 1016–1031.

LE DIZÈS, S. & LAPORTE, F. 2002 Theoretical predictions for the elliptical instability in a two-vortex flow. *J. Fluid Mech.* **471**, 169–201.

LE DIZÈS, S. & VERGA, A. 2002 Viscous interactions of two co-rotating vortices before merging. *J. Fluid Mech.* **467**, 389–410.

LEWEKE, T. & WILLIAMSON, C. H. K. 1998 Cooperative elliptic instability of a vortex pair. *J. Fluid Mech.* **360**, 85–119.

LEWEKE, T. & WILLIAMSON, C. H. K. 2011 Experiments on long-wavelength instability and reconnection of a vortex pair. *Phys. Fluids* **23**, 024101.

KELVIN, LORD 1880 Vibrations of a columnar vortex. *Phil. Mag.* **10**, 155–168.

MARIOTTI, A., LEGRAS, B. & DRITSCHEL, D. G. 1994 Vortex stripping and the erosion of coherent structures in two-dimensional flows. *Phys. Fluids* **6**, 3954.

MARSHALL, J. S., BRANCHER, P. & GIOVANNINI, A. 2001 Interaction of unequal anti-parallel vortex tubes. *J. Fluid Mech.* **446**, 229–252.

MEUNIER, P. & LEWEKE, T. 2005 Elliptic instability of a co-rotating vortex pair. *J. Fluid Mech.* **533**, 125–159.

MOORE, D. W. & SAFFMAN, P. G. 1975 The instability of a straight vortex filament in a strain field. *Proc. R. Soc. Lond.* A **346**, 413–425.

ORTEGA, J. M., BRISTOL, R. L. & SAVAŞ, Ö. 2003 Experimental study of the instability of unequal-strength counter-rotating vortex pairs. *J. Fluid Mech.* **474**, 35–84.

ROY, C., LEWEKE, T., THOMPSON, M. C. & HOURIGAN, K. 2011 Experiments on the elliptic instability in vortex pairs with axial core flow. *J. Fluid Mech.* **677**, 383–416.

ROY, C., SCHAEFFER, N., LE DIZÈS, S. & THOMPSON, M. C. 2008 Stability of a pair of co-rotating vortices with axial flow. *Phys. Fluids* **20**, 094101.

RYAN, K. & SHEARD, G. J. 2007 Nonlinear growth of short-wave instabilities in a Batchelor vortex pair. In *Proceedings of the 16th Australasian Fluid Mechanics Conference, School of Engineering, The University of Queensland* (ed. P. Jacobs, T. McIntyre, M. Cleary, D. Buttsworth, D. Mee, R. Clements, R. Morgan & C. Lemckert). pp. 1463–1469.

SAFFMAN, P. G. 1992 *Vortex Dynamics*. Cambridge University Press.

SCHAEFFER, N. & LE DIZÈS, S. 2010 Nonlinear dynamics of the elliptic instability. *J. Fluid Mech.* **646**, 471–480.

SCORER, R. S. & DAVENPORT, L. J. 1970 Contrails and aircraft downwash. *J. Fluid Mech.* **43** (3), 451–464.

SHEARD, G. J., FITZGERALD, M. J. & RYAN, K. 2009 Cylinders with square cross section: wake instabilities with incidence angle variation. *J. Fluid Mech.* **630**, 43–69.

SIPP, D., JACQUIN, L. & COSSU, C. 2000 Self-adaptation and viscous selection in concentrated two-dimensional vortex dipoles. *Phys. Fluids* **12**, 245.

SO, J., RYAN, K. & SHEARD, G. J. 2011 Short-wave instabilities on a vortex pair of unequal strength circulation ratio. *Appl. Math. Model.* **35** (4), 1581–1590.

THOMAS, P. J. & AUERBACH, D. 1994 The observation of the simultaneous development of a long- and a short-wave instability mode on a vortex pair. *J. Fluid Mech.* **265**, 289–302.

THOMPSON, M. C., HOURIGAN, K. & SHERIDAN, J. 1996 Three-dimensional instabilities in the wake of a circular cylinder. *Exp. Therm. Fluid Sci.* **12** (2), 190–196.

TSAI, C.-Y. & WIDNALL, S. E. 1976 The stability of short waves on a straight vortex filament in a weak externally imposed strain field. *J. Fluid Mech.* **76**, 721–733.

WIDNALL, S. E., BLISS, D. B. & TSAI, C.-Y. 1974 The instability of short waves on a vortex ring. *J. Fluid Mech.* **66**, 35–47.